## Cryogenic characterisation of a permanent magnet stepper motor and its impact on the MICADO atmospheric dispersion corrector

van den Born, Joost; Eggens, Martin; Nieuwenhuizen, Ad; Jellema, Willem; Navarro, Ramon; Jayawardhana, Bayu

# Cryogenic characterisation of a permanent magnet stepper motor and its impact on the MICADO atmospheric dispersion corrector

J.A. van den Born[a,b,c,*], M.J. Eggens[d], A.C.T. Nieuwenhuizen[e], W. Jellema[b,d], R. Navarro[a], B. Jayawardhana[c]

[a]*NOVA Optical Infrared Instrumentation Group at ASTRON, Oude Hoogeveensedijk 4, NL-7991 PD Dwingeloo, the Netherlands*
[b]*Kapteyn Astronomical Institute, University of Groningen, PO Box 800, NL-9700 AV Groningen, the Netherlands*
[c]*Engineering and Technology Institute Groningen, University of Groningen, Nijenborgh 4, NL-9747 AG Groningen, the Netherlands*
[d]*SRON Netherlands Institute for Space Research, PO Box 800, NL-9700 AV Groningen, the Netherlands*
[e]*SRON Netherlands Institute for Space Reseach, Niels Bohrweg 4, 2333 CA, Leiden, The Netherlands*

## Abstract

The MICADO atmospheric dispersion corrector (ADC) will be the first ADC built for an astronomical instrument that has to operate in a cryogenic environment ($T = 77$ K). A detailed understanding of the system behaviour is necessary to maximise the operational lifetime of the planned design concept and to design a suitable controller. The MICADO ADC design features a friction drive concept that is powered by a commercially available permanent magnet stepper motor (PMSM). Here, we report on an extensive characterisation of this PMSM. By matching the experimental results to an analytical description of PMSMs, we obtain a solid foundation to build a complete dynamical model of the ADC system. A prototype of the ADC design concept had already been built and tested at its operational temperature. The results from these tests allowed us to compare the measured and modelled response and discuss the implications. With respect to the motor characterisation, we find no significant performance difference of the tested stepper motor when operated at room temperature, compared to at 77 K. However, we do find that static friction plays a large role in the precise response of the ADC mechanism.

*Keywords:* Stepper motors, Experimental, Modeling, Astronomical instrumentation, Cryogenic.

## 1. Introduction

MICADO, the Multi-AO Imaging CamerA for Deep Observations, is one of three astronomical instruments in development for the Extremely Large Telescope (ELT) [1–3]. It is a near-infrared imaging camera and spectrograph that will serve a broad range of astronomical science. The instrument will make use of an atmospheric dispersion corrector (ADC) to reduce the effect of atmospheric dispersion [4] – the differential refraction of light at different wavelengths as it passes through Earth's atmosphere [5]. By accurately positioning two sets of prisms the magnitude and direction of the correction vector can be tuned. On an ELT class telescope, the precise positioning of these amici prisms is of much higher importance as compared to current observatories, due to the much higher spatial resolution that is provided by the large primary mirror [4, 6].

The design of the MICADO ADC consists of two nearly identical mechanisms, that both position a prism pair independently. In each mechanism, the optics combine with the rotor of the angular encoder, the aluminium mount and structural support, to form the rotating body. Three smaller roller wheels act as bearings to the larger rotor wheel, one of which is powered

by an electrical motor. The mechanical design features a stepper motor to position the ADC prism pair.

Two-phase permanent magnet stepper motors (PMSM) are a very popular type of electric motor, due to their large and immediately available torque, simple – but accurate – open loop control and low price. Specialised PMSM have been developed for cryogenic [7, 8] and space environments [9–11], and these are also commercially available [12, 13][1]. For the MICADO ADC, off-the-shelf PMSM from Phytron are used, which are compatible with the cryogenic environment (77 K, vacuum) in which the MICADO ADC will operate.

Unfortunately, the cryogenic performance of PMSM are not well described in literature and the data sheets provided by the manufacturer usually describe the performance at room temperature only. Existing literature often focuses on thermal and power losses for deep cryogenic temperatures [14], or considers different types of electric motors [15–17]. Also, the performance of stepper motors is often evaluated at moderate to high rotation rates (> 100 rpm). In contrast, the motors of the ADC will primarily operate in the low step frequency regime during astronomical observations with MICADO. This low stepping frequency results from the mechanical design, where only a small gear ratio of approximately 6.3:1 exists between the motor axis and the rotor wheel, and from the slow evolution of

---

*Corresponding author at: NOVA Optical Infrared Instrumentation Group at ASTRON, Oude Hoogeveensedijk 4, NL-7991 PD Dwingeloo, the Netherlands.

*Email address:* `born@astron.nl` (J.A. van den Born)

---

[1]There are several other manufacturers that can make similar stepper motors for use in cryogenic and space environments, such as FAULHABER, Cobham Advanced Electronic Solutions (CAES) and Lin Engineering.

the atmospheric dispersion vector. For example, a typical two minute observation with MICADO requires the ADC prisms to rotate by roughly 0.6°, corresponding to only two full steps of the stepper motor.

Before an algorithm for the positioning of the ADC can be implemented and a suitable controller can be designed, we need to understand the system behaviour in detail. Fundamentally, the design of MICADO is such that the ADC can not be controlled in closed loop through direct optical feedback, because the error signal – the residual dispersion – is small enough that it cannot easily be measured unless the science image is significantly altered [4, 18, 19]. Therefore, the positioning of the ADC optics must rely on a model that provides the desired configuration or reference signals. Based on the computed reference signals from the model, the positioning of the prisms can then be done in a closed loop, with feedback from the angular encoders.

A thermal and mechanical prototype of the ADC mechanism was built and tested by the NOVA Optical Infrared Instrumentation Group at ASTRON. While the initial performance was excellent, considerable wear-related issues occurred during testing of the desired ten year lifetime [4, 20]. Although these issues were mostly resolved through optimisations of materials, there remained a desire to better understand the physical cause of these issues and to avoid similar difficulties in the future.

With these objectives in mind, we developed a model that accurately describes both the behaviour of the motor, as well as the complete ADC mechanism, in the cryogenic environment where the system will nominally operate. This model helped us to achieve a deeper understanding of the observed performance of the ADC mechanism prototype. For the first part of this article, we have carried out an extensive characterisation of the Phytron VSS43.200.1.2 cryogenic PMSM that we will use in the MICADO ADC, both at room temperature and within a cryogenic environment ($T$ = 77 K). The theory of stepper motors is described in Section 2. Then, we use empirical measurements to match the analytic description to the real motor. The experimental setup and results are discussed in Section 3. In the second part of this paper, the representative motor model is implemented into a complete dynamical description of the ADC in Section 4. We compare the simulated response of the combined model directly to the detailed response measured on the prototype and study the similarities and differences. Finally, we discuss the repercussions of our findings and some considerations for the design a suitable controller in Section 5.

## 2. Cryogenic Permanent Magnet Stepper Motors

### 2.1. Dynamics of a Permanent Magnet Stepper Motor

The dynamics of a two phase stepper motor are derived in [21] and summarised by the following differential equations,

$$
\begin{aligned}
\frac{di_1}{dt} &= -\frac{R}{L_0}i_1 + \frac{k_m}{L_0}\omega \sin(N_r\theta) + \frac{v_1}{L_0}, \\
\frac{di_2}{dt} &= -\frac{R}{L_0}i_2 - \frac{k_m}{L_0}\omega \cos(N_r\theta) + \frac{v_2}{L_0}, \\
\frac{d\omega}{dt} &= \frac{1}{J}(\tau - \tau_l - B\omega), \\
\frac{d\theta}{dt} &= \omega.
\end{aligned}
\tag{1}
$$

The first two lines describe the electrodynamics of a PMSM. The currents ($i_1$, $i_2$) or the voltages ($v_1$, $v_2$) can be used as the input for the two phase stepper motor. The resistance and inductance of the coils are given by $R$ and $L_0$, respectively. The third and fourth lines in this set of equations describe the mechanical dynamics. The rotor angular position and angular velocity are denoted by $\theta$ and $\omega$. The parameter $J$ is the inertia experienced by the motor. Any load might enact a torque on the system, here denoted by $\tau_l$. Then, $B\omega$ is the friction torque, with $B$ the viscous friction coefficient. Finally, $k_m = N_r L_{m1} i_f$ is the torque constant, defined by the number of poles on the rotor, $N_r$, the mutual inductance between the permanent magnet in the rotor and the coils, $L_{m1}$, and the imaginary current that flows through the coils due to the flux from the permanent magnet, $i_f$. The torque $\tau$ delivered by the motor is described by

$$
\tau = k_m \left[-i_1 \sin(N_r\theta) + i_2 \cos(N_r\theta)\right]
$$
$$
- 2L_{f4}N_r \sin(4N_r\theta)i_f^2. \tag{2}
$$

The first term describes the main driving torque of the motor as an input current is fed into it. The last term in this expression is the detent torque of the motor, which is a resisting torque that exists even when the motor is not powered on and which is governed by the electromagnetic interaction between the rotor and stator poles, where $L_{f4}$ is the fourth harmonic of the mutual inductance between the stator and rotor poles.

Another useful property of stepper motors is the holding torque. The torque required to move the rotor as a constant current, the holding current, is fed into one or both of the phases A and B. Under the assumption that the powered torque is much larger than the detent torque, the holding torque is given by

$$
\tau_h = k_m \sqrt{i_1^2 + i_2^2}. \tag{3}
$$

### 2.1.1. Micro-stepping

Micro-stepping is used to more precisely rotate the rotor than is possible with full stepping. In micro-stepping, the input currents follow a sinusoidal shape, using a discrete number of phase angle shifts. The second phase has a $\pi/2$ phase delay relative to the first phase. Thus, the input currents $i_1$ and $i_2$ can be given by

$$
\begin{aligned}
i_1 &= i_m \cos\phi, \\
i_2 &= i_m \sin\phi,
\end{aligned}
\tag{4}
$$

where the motor current amplitude $i_m$ is a fixed constant that forms the radius of the phase diagram and $\phi$ denotes the phase angle. The resolution of the microstep determines the discontinuous incremental increase in the phase angle. In general, for a step resolution $1/n$, we find that

$$\delta\phi = \frac{2\pi}{4n}. \tag{5}$$

For each period of the input signal, the motor performs four full motor steps. The number of microsteps per full rotation of the motor axis is $4N_rn$.

## 2.2. Experimental approach

The theoretical model of equation (1) has been extensively described in other works [21–24] and we assume its validity. Some of the parameters in the differential equations can be measured directly, such as the resistance ($R$), inductance ($L_0$), current ($i$) and voltage ($v$). Then, there are several parameters that can be retrieved from the design of the motor (e.g. the inertia $J$ of the motor rotor) or that can be estimated without a major penalty (e.g. the viscous friction coefficient $B$). The remaining parameters can be derived from easily measurable performance metrics.

The torque constant $k_m$ can be found as the linear coefficient of the holding torque as a function of increasing current. The peak detent torque $\tau_d^{\max}$ can be determined from the required torque to move the motor axis by at least a full step, and independently as the offset of the linear torque-current relation. From the measurement of the torque constant ($k_m = N_rL_{m1}i_f$) and the maximum detent torque, given by

$$\tau_d^{\max} = 2L_{f4}N_ri_f^2, \tag{6}$$

we relate the magnitude of $L_{f4}$ to $L_{m1}$ using the imaginary current induced by the permanent magnet $i_f$ that appears in both expressions. This leads to

$$L_{f4} = \frac{\tau_dN_r}{2k_m^2}L_{m1}^2. \tag{7}$$

This scaling relation has the useful consequence that $i_f$ becomes irrelevant for the modelled behaviour of the motor, as long as this scaling is adhered to. In our modelling, we set $i_f$ to equal one, which effectively removes $i_f$ from the constants $L_{m1}i_f$ and $L_{f4}i_f^2$.

Finally, we did not directly measure the viscous friction coefficient $B$. The effect of this coefficient is most important at large angular velocities and high stepping rates. Because we are primarily interested in the behaviour of the motor in the context of the ADC prism positioning, thus operation of the motor at low stepping rates, the role of $B$ will be marginal. In Section 4.3 we will determine an empirical value for $B$ for the combined motor and ADC system.

## 2.3. Test setup description

To characterise the cryogenic Phytron VSS43.200.1.2 PMSM used for the MICADO ADC, we applied a classical
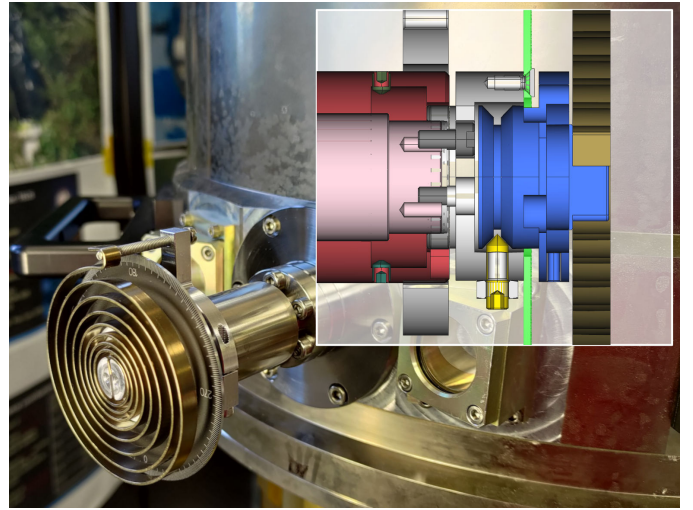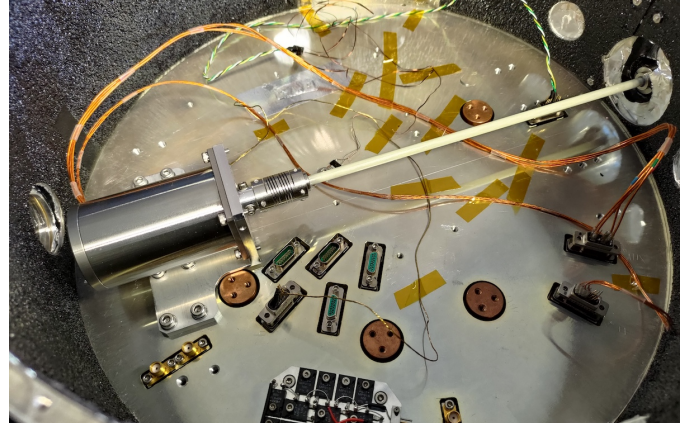


Figure 1: Overview of the test setup. Top picture: The PMSM is connected to the outside by a glass fiber axis, where two axial couplings accommodate small misalignment between the motor axis and the rotary feedthrough. Bottom picture: The rotary feedthrough and the clock spring mechanism. The inset shows the design of this mechanism. The shell of the rotary feedthrough (red) co-rotates with the motor axis. When the clock spring (brown) is fixed in position with set screws (yellow), the motor will displace the outer radius of the spring. Conversely, if the set screws are loosened, the clock spring mechanism can be rotated and a desired torque is applied to the motor.

technique to measure torque; through the angular excitation of a clock spring. Two differently sized clock springs were used. A smaller clock spring, with a lower specified torsion constant (0.26 mNm/deg), was chosen to measure the specified 7 mNm detent torque of the Phytron motor. The larger clock spring had a higher specified torsion constant (0.83 mNm/deg), more suited to the higher holding and driving torque of the motor.

For this experiment, we used a cryostat with a cold bench inner diameter of 320 mm, to which the Phytron VSS43.200.1.2 stepper motor was fixed using an adapter plate. A 215 mm long glass fiber axis with axial couplings on either side provided margin for axial misalignment. Temperature sensors were located on the adapter plate, the cold bench and in the motor internals, near the stator coils. The torque delivered by the motor was transferred through a magnetically coupled rotary feedthrough. We designed a mechanism, that could either rotate with the motor axis or be fixed in place, illustrated in the
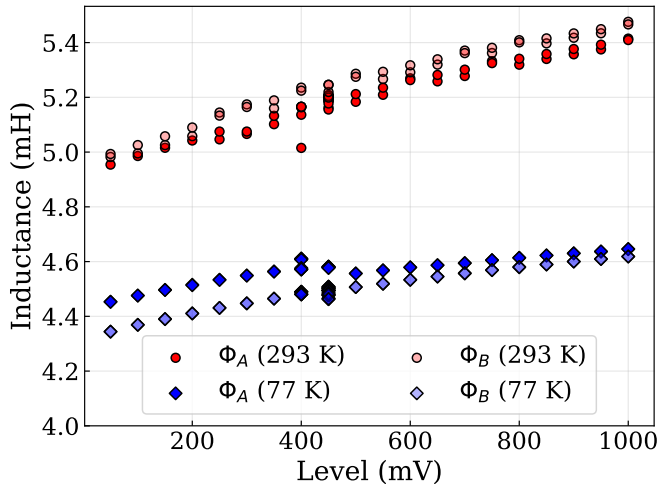
Figure 2: The measured motor inductance as a function of AC voltage. The inductance varies with the supplied voltage of the test signal ($f$ = 1 kHz), but starts to saturate at 77 K. The inductance drops from around 5.2 mH at room conditions to 4.5 mH at 77 K.

bottom panel of Fig. 1. This mechanism was attached to the rotary feedthrough on the outside of the cryostat. By rotating the wheel of the mechanism, the detent and holding torque of the motor could be tested. If instead the wheel was fixed, rotation of the motor would wind up the clock spring until the driving torque was exceeded and the motor would jump back to a position of lower potential energy.

The experiment was carried out in March of 2022 and the analysis was done in subsequent months.

## 3. Characterisation of a cryogenic PMSM

### 3.1. Inductance

The inductance of the two motor phases was measured with an Agilent 4263B LCR meter, which provided an alternating current (AC) test signal to determine the inductance. From the four available test frequencies, a test frequency of 1 kHz provided the most consistent results. In addition, at this frequency the room temperature measurements agreed well with the 5.2 mH value that was given in the motor specifications. Therefore, this signal frequency appears representative for the operation of the motor. The inductance was measured for both phases at twenty different voltage levels in the range 50-1000 mV, first at 293 K and again at 77 K. The recorded values are presented in Fig. 2.

In this figure, three observations can be made. The first is the decrease in the motor winding inductance by 0.7 mH, relative the room temperature, to an average value of 4.5 mH. A decrease of the inductance with decreasing temperature is not immediately obvious and we will discuss it momentarily. Second, the cryogenic inductance value appears to taper off as the voltage increases. This behaviour does not occur at room temperature. Finally, the differential inductance between the two motor phases appears to have switched. We belief that this was most likely a bookkeeping error.

A rigorous and fundamental derivation of the relationship between the inductance $L$ and temperature $T$ is outside the scope of this work. However, the fact that the Agilent 4263B LCR meter provides an AC signal, points to the skin effect as a relevant effect. This effect describes how most electromagnetic current flows primarily near the surface of a conductor, because induced eddy currents decrease the field strength proportional to the distance away from the conductor boundaries. The skin depth $\delta$ provides a measure for the skin effect and is defined as the depth where $1/e$ of the field strength is left [25]. It is given by

$$\delta = \sqrt{\frac{\rho}{\mu_0 \mu_r \pi f}}, \tag{8}$$

where $f$ is the frequency of the alternating current and $\rho$ is the resistivity of the conductor. When the skin effect is present, then the effective area through which the magnetic field flows decreases, in turn decreasing the total effective flux within the solenoid and therefore the inductance, as compared to when a DC current is applied.

Because the resistivity scales with temperature, it becomes clear how the inductance may scale with temperature, qualitatively explaining the observed difference illustrated in Fig. 2.

The skin effect also explains why we might see saturation in the inductance of the cold motor coils and not in the room temperature measurements. Because the effective area decreases with temperature, and because the eddy currents increase the field slightly in this region, the point of magnetic saturation is reached earlier at lower temperatures. Finally, that we see magnetic saturation for the measurements at 77 K, specifically, and not for those at 293 K, is related to the relative magnetic permeability of the stator core material, the geometry of the rotor stator, the material properties and the test signal properties.

### 3.2. Resistance

The electrical resistance of the phase wiring to a direct current was measured using the Agilent 34970A LCR meter and separately by a multimeter. The lead dioxide ($PbO_2$) wiring internal to the cryostat has a significantly higher resistance – and worse thermal conductivity – than the copper wire used for motor. By measuring the combined resistance of the cryostat and motor wiring, and also a separate cryostat wiring loop, we could derive the resistance of the motor wiring at different temperatures.

A scatter plot of the measured values is presented in Fig. 3. The resistance of the motor wiring changed from 2.6 $\Omega$ at room temperature to 0.5 $\Omega$ at 77 K, in line with the changing copper resistivity [26]. The combined resistance dropped from 9.4 $\Omega$ to 6.5 $\Omega$. Some linear variations in the measured data were noted, caused by thermal drift of the motor or the cold bench. This is particularly apparent in the leftmost inset of Fig. 3, where the motor was actively being used while recording the resistance data.

### 3.3. The torsion constant of the clock springs

Before measuring the detent torque, holding torque and driving torque of the motor, we verified the torsion constant of the
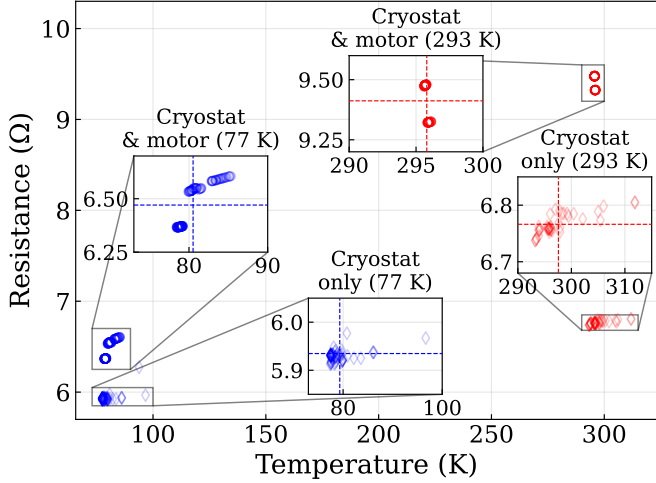
Figure 3: The measured DC resistance of the motor and cryostat wiring at warm (293 K, red) and cryogenic (77 K, blue) conditions. The wiring through the cryostat was measured separately to disentangle the motor wiring resistance from the combined resistance of the complete setup.
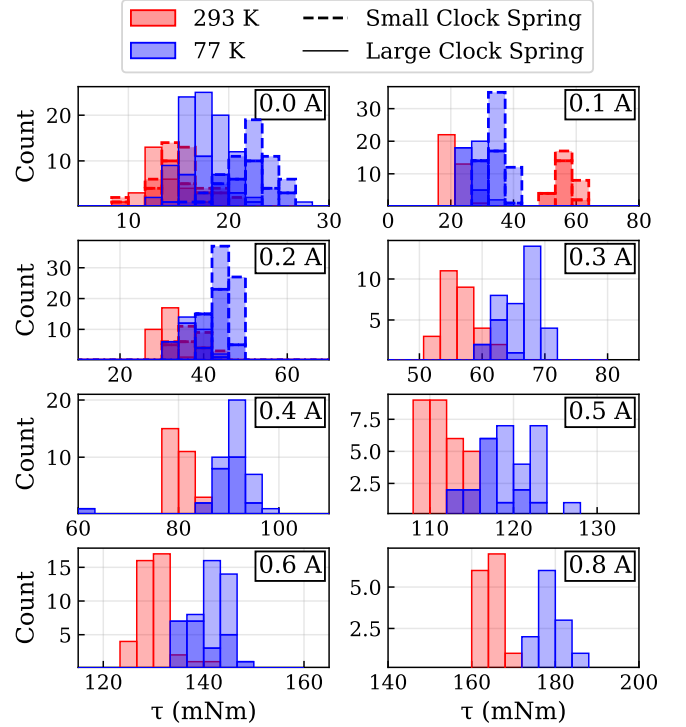


Figure 4: The measured holding torques at eight different current levels. The cold motor (blue) shows consistently higher holding torque levels, compared to when the motor is at room temperature (red). Below 0.3 A, both clock springs were used to measure the holding and detent torque. Each bin is a stack of two different shades, corresponding to one of two directions (clockwise or counter clockwise) in which the torque was applied.

springs. To calibrate the conversion of angular excitation of the clock springs to a measured torque, we determined the torsion constant of the clock springs from their damped harmonic oscillation after excitation with a small weight. An ASUS ZenFone 8 smartphone recorded the oscillations at >300 frames per second, we processed the video using the open-source video analysis software Kinovea [27] and the derivation of the torsion constant was done in Python. To find the torsion spring constant, we assumed the underdamped harmonic oscillator response in angular form,

$$\theta(t) = A e^{-\zeta \omega_0 t} \sin\left(\omega_0 t \sqrt{1 - \zeta^2} + \phi\right). \tag{9}$$

The undamped angular frequency $\omega_0$ is defined through the inertia $J$ acting on the spring and the torsion constant $\mu$ of the spring itself,

$$\omega_0 = \sqrt{\frac{\mu}{J}}. \tag{10}$$

The damping ratio $\zeta$ is a function of the rotational friction $B$, the inertia $J$ and the torsion spring constant $\mu$.

$$\zeta = \frac{B}{2} \sqrt{\frac{1}{J\mu}}. \tag{11}$$

The constants $A$ and $\phi$ denote the amplitude and phase shift to match the initial conditions of the response.

Based on this procedure, we chose to adopt $\mu_{small} = 0.229 \pm 0.017$ mNm/deg for the small clock spring and $\mu_{large} = 0.665 \pm 0.025$ mNm/deg for the larger clock spring. For a more detailed description of the spring torsion constant verification, see Chapter 5 in [20].

### 3.4. The holding torque and detent torque

For the measurement of the detent and holding torque, the set screw on the clock spring mechanism, see Fig. 1, was loosened

and a torque was applied by slowly exciting the clock spring. At some point the torque of the spring exceeded the resisting motor torque and the motor axis would move. The angular position of the spring, at the moment that this happened, provided a value for the measured performance.

In total, 228 separate measurements were performed with the motor in an unpowered state, of which 75 at room temperature and 153 at 77 K, respectively. The holding torques were tested at 0.1, 0.2, 0.3, 0.4, 0.5, 0.6 and 0.8 A. At currents larger than 0.2 A it was not possible to accurately determine the holding torque using the smaller clock spring. Therefore, only the larger clock spring was used at higher current amplitudes. Histograms of the measured values are presented in Fig. 4.

In our measurements, we detected no significant directional bias of the motor axis rotation. However, there seemed to be some disagreement in the measured detent torque when comparing the small spring against the large spring. When a holding current is present, this discrepancy decreased. Perhaps, this could result from a non-linearity of the spring at small excitation angles. The measured holding torque is consistently larger when the motor is in the cryogenic environment as compared against room temperature.

In equation (3), we neglected to include the detent torque. Therefore, we performed a linear best fitting to the data based on that expression, but allowed for a non-zero offset at a holding current of zero. Doing so, we found the torque constant $k_m$ and
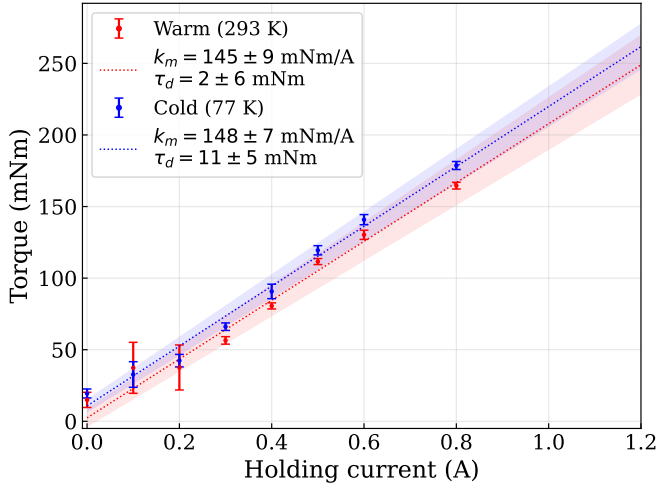
Figure 5: The measured holding torques and the best fit up to the rated motor current of 1.2 A.

the detent torque $\tau_d$. At room temperature, our best estimates were $k_m = 145 \pm 9$ mNm/A and $\tau_d = 2 \pm 6$ mNm. Similarly, our best estimates at 77 K were $k_m = 148 \pm 7$ mNm/A and $\tau_d = 11 \pm 5$ mNm. These findings are illustrated in Fig. 5.

Unfortunately, we could not yet exclude the possibility that the performance did not change at all, due to the limited number of data points. However, the consistency with which our measurements show improved performance at cryogenic temperatures does suggest a slight increase in the holding torque of a few percent.

### 3.5. Driving torque

The driving torque is usually an important selection criterion when choosing a motor. In contrast to the previously discussed parameters, it is not required to be able to model the motor behaviour. Nonetheless, we present here a limited exploration of the parameter space containing the stepping rate, stepping mode and driving current. The stepping rates $f_s$ and stepping modes $n$ were chosen such that multiple combinations could be made at the same current frequency $f_c$, following

$$f_c = \frac{f_s}{4n}. \tag{12}$$

Usually, the parameter that can be chosen in the motor controller is the stepping rate and not the current frequency.

As with all previous measurements, they were performed both at room temperature (293 K) and pressure and in a vacuum at a cryogenic temperature of 77 K. We explored the performance at 0.2, 0.5 and 0.9 A. For each step frequency, the microstepping was varied between full stepping and 1/32 microstepping. The stepping rates ranged from 100 Hz to 3200 Hz.

Rotation of the clock spring was prohibited by lowering the set screws on the clock spring mechanism, shown in yellow in Fig. 1. When the motor was active, it wound up the spring increasing the load torque. After some amount of rotation the potential energy stored in the spring exceeded the maximum

torque that could be delivered by the motor and the forward rotation would cede. In practice, the motor would be pushed back violently due to the absence of a holding current, which was set to 0 A because of thermal considerations. As with the spring calibration, the interaction between the motor and the spring was recorded using an ASUS ZenFone 8 smartphone at >300 frames per second. A total of 228 videos were recorded, processed in the open-source video analysis software Kinovea [27] and the resulting data was analysed in Python. From each video a time-position curve was extracted, where the maximum deviation was determined relative to the angular position at which the spring was relaxed. An arbitrarily chosen threshold was set at 88 per cent of the maximum deviation to find all torque peaks in the time-position curve, without including the violent oscillations that occured after the maximum motor torque was exceeded. The retrieved maxima were then averaged to find a practical value and a standard deviation of the maximum driving torque. In most cases, this method provided a small number of torque values corresponding to the maximum torque provided by the motor. In several cases, the motor showed erratic behaviour and provided little torque. However, this meant that the analysis code found many maxima above the set threshold.

A complete overview of the measured driving torques is given in Appendix C. We note that the holding torque is generally significantly higher than the driving torque. This can be explained by considering that the two phase currents are at a $\pi/2$ phase difference during normal operation. At equal current amplitude for both phases, the motor torque in equation (2) scales directly with the current amplitude. For the holding torque, because both phases are powered simultaneously, the relation scales with $\sqrt{2}$ times the current amplitude. At 0.5 A and 0.9 A this did indeed fairly closely agree with our data. At 0.2 A the difference between the driving torque and the holding torque was significantly larger than a factor of $\sqrt{2}$, even when accounting for the detent torque, suggesting that there was some unknown measurement inaccuracy or systematic error at low driving currents. Possibly, the oscillations of the clock springs that occurred when the motor was active are responsible, which made the point of maximum torque somewhat inconsistent.

### 3.6. Simulated temporal response of the warm and cold motor

Table 1 summarises the measured and derived motor parameters. Our findings at 293 K are consistent with the manufacturer provided specifications. At 77 K, only $L_0$, $R$ and $\tau_d$ have changed appreciably relative to room temperature.

We will now compare the motor response using these parameters. The temporal response is modelled through the equations provided in Section 2.1. The differential equations are solved either numerically by using small time steps and letting the response evolve or semi-analytically using the `solve_ivp()` function in SciPy [28]. In the latter an explicit Runge-Kutta method [29] is used for a voltage input. Alternatively, an implicit Runge-Kutta method [30] is used for a current input. Numerical experimentation showed that the results were most consistent using these two methods. Provided with sufficient temporal sampling, the numerical time evolution and the semi-analytic solution to equation (1) provide identical results.

Table 1: This table summarises the results of the measured and derived motor parameters. Values within brackets are not measured or provided, but assumed realistic.

| Param. | Unit | 293 K | 77 K | Spec. | |
|---|---|---|---|---|---|
| $L_0$ | mH | 5.2 | 4.5 | 5.2 | |
| $R$ | $\Omega$ | 2.6 | 0.5 | 2.6 | |
| $N_r$ | | 50 | 50 | 50 | * |
| $J$ | kg m$^2$ | – | – | $7.7 \times 10^{-6}$ | |
| $B$ | mNm s deg$^{-1}$ | $(3.5 \times 10^{-3})$ | $(3.5 \times 10^{-3})$ | $(3.5 \times 10^{-3})$ | |
| $k_m$ | mNm A$^{-1}$ | $145 \pm 9$ | $148 \pm 7$ | 138 | |
| $L_{m1}$ | mH | $2.91 \pm 0.12$ | $2.96 \pm 0.10$ | 2.77 | † |
| $L_{f4}$ | mH | $< 0.06$ | $0.11 \pm 0.05$ | 0.07 | ‡ |
| $i_f$ | A | 1 | 1 | 1 | § |
| $\tau_h$ | mNm | $246 \pm 14$ | $251 \pm 12$ | 235 | ‖ |
| $\tau_d$ | mNm | $2 \pm 6$ | $11 \pm 5$ | 7 | |

* Fixed by design.
† Derived from the torque constant, $k_m = N_r L_{m1} i_f$.
‡ Derived from equation (7), under the assumption that $i_f = 1$ A.
§ Set to 1 A.
‖ Holding torque with both phases powered at the rated motor current. The value excludes the contribution of the detent torque. Computed from $\tau_h = k_m \sqrt{2} i_h$, where $i_h = 1.2$ A.



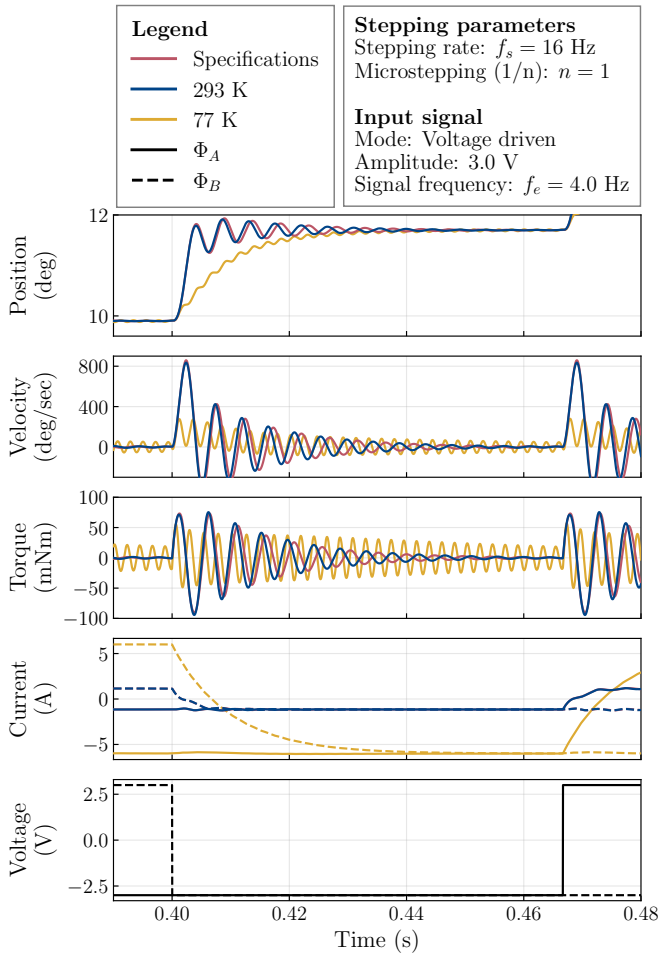| Legend | | Stepping parameters |
|---|---|---|
| | Specifications | Stepping rate: $f_s = 16$ Hz |
| | 293 K | Microstepping $(1/n)$: $n = 1$ |
| | 77 K | **Input signal** |
| | $\Phi_A$ | Mode: Voltage driven |
| | $\Phi_B$ | Amplitude: 3.0 V |
| | | Signal frequency: $f_e = 4.0$ Hz |

Figure 6: In this figure, we compare the temporal response of the motor as specified, as measured at room temperature (293 K) and as measured at cryogenic (77 K) temperatures. The model parameters are provided in Table 1. The stepping parameters and input signal are specified in the figure.

For the electrical input of the motor, we can choose to provide a current or voltage signal. One is converted into the other in the simulation through Ohm's law, including a counter-electromotive force component. If the input signal is a step function, as is approximated when the motor is moved in full stepping mode, then the response of the electric counterpart is slightly delayed, described by the electrical time constant

$$t_e = \frac{L}{R}. \tag{13}$$

One example is illustrated in Fig. 6. Here, we have detailed the simulated temporal response in terms of position, velocity and torque of the motor. We compare the motor as specified by the manufacturer, to the as-measured warm and cold motor. For the input, we used a full stepping voltage signal, with an amplitude of 3 V. The cold motor also takes much longer to move by the desired 1.8°. This is due to the much lower resistance, which has increased the electrical time constant significantly. The lower inductance further reduces $t_e$. The longer $t_e$ can also be seen in the curve of the induced current, where the current in the cold motor requires much longer than the warm motor to drop from its maximum to its minimum value.

The response simulated in Fig. 6 shows that the warm as-measured motor performs very similar to the specifications, with only a very minor change in the resonant frequency. The cold as-measured motor response shows a slightly different resonant frequency. The different values of $L_{m1}$ are the cause of this different resonant frequency. If a PMSM is treated as an harmonic oscillator, then the resonant frequency $f_0$ can be shown to equal [21, 31]

$$f_0 = \left[ \frac{2N_r^2 L_{m1} i_f \sqrt{i_1^2 + i_2^2}}{8\pi^2 J} \right]^{1/2}. \tag{14}$$

In this expression, $L_{m1}$ is the only parameter that differs between the three simulated motor responses.

Next, we compared the voltage driven input signal against the current driven input signal for three different stepping modes. By choosing the amplitudes of the signal, such that they convert into each other through the resistance of the warm motor, we could make a fair comparison. Fig. 7 gives the resulting positioning response for the three simulated motors. Immediately, large oscillations appear when driving the motor through a current input signal. The oscillations are still controlled, as all motors reach their final position at roughly the same time in the figure. The cold motor arrives slightly later, due to the aforementioned larger time constant. At higher microstepping modes, the angular rotation per unit time approaches a straight line in both current and voltage driven modes.

## 4. ADC system description

With the analytic model of our Phytron VSS43.200.1.2 cryogenic stepper motor in hand, we return to the MICADO atmospheric dispersion corrector (ADC) and look at the behaviour of the whole system as a whole. First, we succinctly describe the
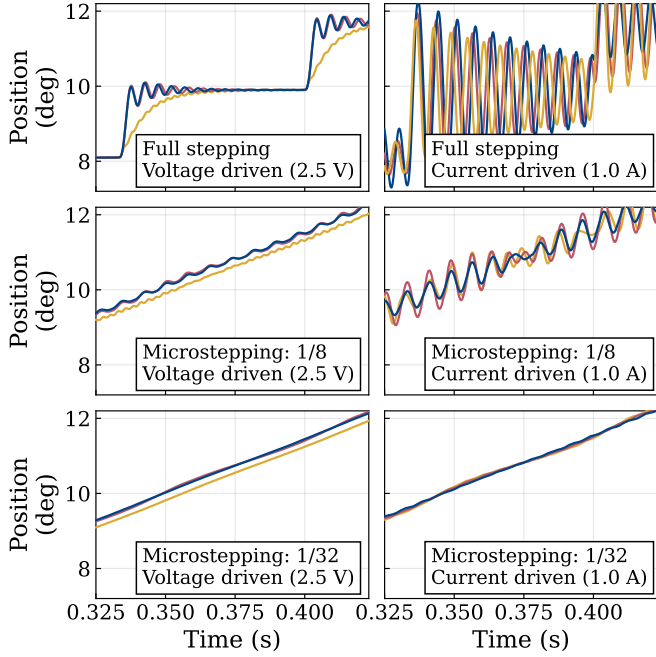
Figure 7: The PMSM dynamics of equation (1) allow for a voltage or current based input signal, which will result in a different response of the motor. Shown here is the motor response for full stepping, 1/8 and 1/32 microstepping modes, with a fixed voltage signal (left column) or fixed current signal (right column). The red lines show the response of the as-specified motor, the as-measured warm motor is shown in blue and the yellow line corresponds to the as-measured cold motor.

ADC mechanism prototype that we have used as a real-world reference for our models. Next, we provide a description of the ADC mechanism without the motor. A derivation of this description is given in Appendix A. Then, in Section 4.4, we combine the motor and ADC mechanism model to analyse the complete system.

### 4.1. The ADC mechanism prototype

A prototype of the ADC mechanism was built and extensively tested for the validation of design assumptions and verification of subsystem requirements [20]. It is shown in Fig. 8. This prototype was a mechanical and thermal representation of the design concept, and contained no optics. Primarily, it was used to obtain experience with the friction drive concept, where three small roller wheels both carry and drive the larger rotating body, in the operational cryogenic (77 K) environment. No gears or belts are used for the transfer of torque, but instead the design relies on the friction between the contact area of the wheels. One of the three roller wheels is driven by the Phytron VSS43 stepper motor. A Zettlex 22-bit absolute angular encoder provides angular position data of the rotor at a resolution of 0.3 arcseconds at a maximum rate of 1 kHz. A gear ratio of 6.3125:1 translates a 1.8° motor step into a rotor reconfiguration of 0.285°.

### 4.2. Fundamental system description of the ADC

In its most basic form, the system consists of one large rotor wheel, three identical small roller wheels and an axial coupling,
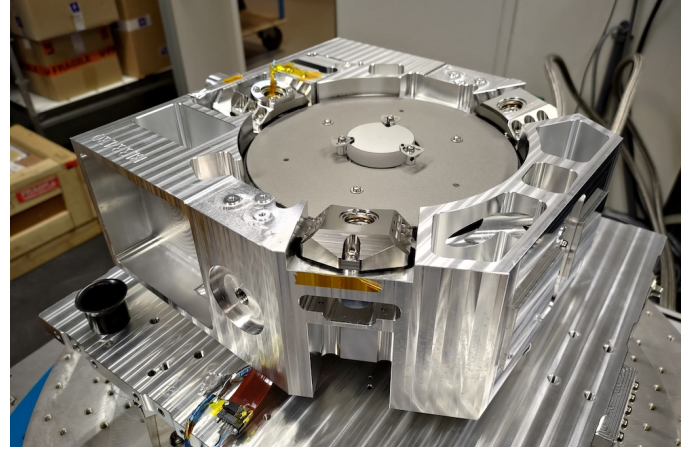


Figure 8: The MICADO ADC mechanism prototype, a thermomechanical representation of the conceptual design. Three smaller bearing wheels both carry and drive the larger rotor wheel in the middle. The roller wheel in the top-left is driven by a Phytron stepper motor.

that connects one of the rollers to the motor. We assume negligible slip or backlash between the small and large wheels. Then, the system can be described by

$$\alpha\ddot{\theta}_2 + \beta\dot{\theta}_2 + \gamma\theta_2 = \theta_m, \tag{15}$$

where

$$\begin{aligned}
\alpha &= -\frac{N}{K}(J_1 + J_3 + J_4) - \frac{J_2}{KN}, \\
\beta &= -\frac{N}{K}(B_1 + B_3 + B_4) - \frac{B_2}{KN}, \\
\gamma &= -N.
\end{aligned} \tag{16}$$

In the above, $\theta_m$ and $\theta_2$ denote the position of the motor axis and the ADC rotor. $J_i$ and $B_i$ are the inertia and viscous friction coefficient of wheel $i$, respectively. Here, wheels 1, 3 and 4 are the three roller wheels, while wheel 2 corresponds to the ADC rotor. $K$ is the torsion constant of the axial coupling and $N$ gives the gear ratio between the roller and rotor wheels.

### 4.3. Damped oscillatory response of the prototype

Equation (15) contains many parameters that need to have a value assigned before the system can be simulated. The gear ratio $N$ and the wheel inertia can be approximated from the mechanical design of the ADC. The friction coefficients and torsion spring constant $K$ of the axial coupling could be estimated from the ADC mechanism prototype. The high temporal and angular resolution of the angular encoder was easily able to record the small oscillatory settling that occurs after a full motor step has completed. The electrical input signal to the motor had turned off by that time, and the settling therefore represented a perturbed system response.

Repeating the procedure described in Section 3.3, we used the underdamped harmonic oscillator equation, equation (9), to find representative values of $B$ and $K$. Our measurement data contained 2000 individual steps. The equilibrium position after each step was set to correspond to a position value of zero, so that equation (9) applied, as shown in Fig. 9. The
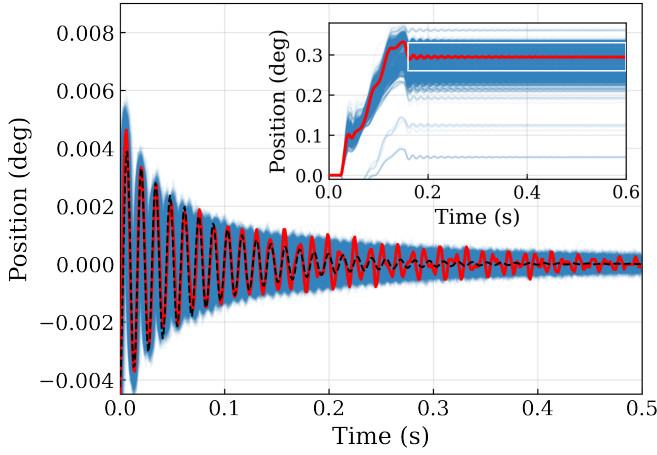
Figure 9: From the measured response of the ADC mechanism prototype, we use the settling behaviour after a full motor step (here, 32 microsteps) has been done. The inset shows the full set of 2000 steps. The white rectangle here shows the part of the step displayed in the main panel. The final position of each step has been set to zero and acts as the equilibrium point. The black dashed line is the best fit of equation (9) to the highlighted step in red.
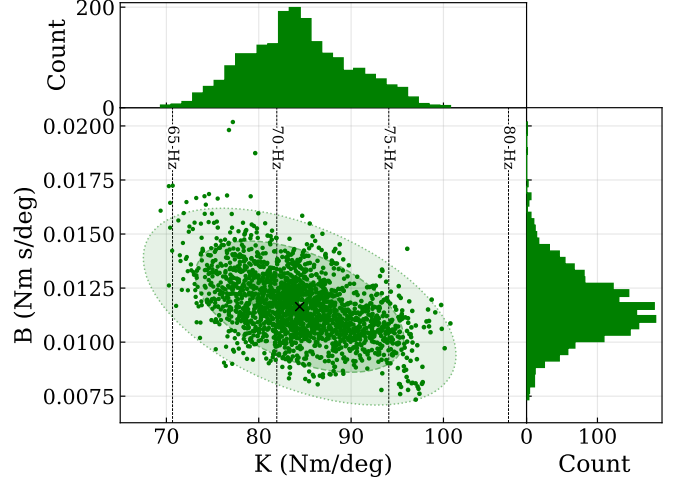
Figure 10: For each individual step, the damped harmonic oscillatory response is used to find the torsion spring constant $K$ and the viscous friction coefficient $B$. Several resonance frequencies of this oscillation are shown through the black dashed lines. The mean value (black cross) is encircled by the $1\sigma$, $2\sigma$ and $3\sigma$ confidence intervals.

best fitting results are presented in Fig. 10. We found that $K = 84.4 \pm 5.6$ Nm/deg and $B = 0.0116 \pm 0.0015$ Nms/deg, with a corresponding resonance frequency of 71.5 Hz.

The found value of $K$ could not be implemented directly, as the axial coupling was not located at the large rotor wheel of the ADC, where the response was measured. Instead, it had to be converted to the coordinate frame of the small rotor wheel that is driven by the motor using the gear ratio. Thus,

$$K_{\text{coupling}} = \frac{K}{N^2}. \qquad (17)$$

The measured value of $B$ did not need to be changed, if we assumed that the friction occurs at the large wheel in the model. In other words, $B_2 = B$ is an effective viscous friction coefficient. Where the friction occurs is not relevant for the model as it pertains to the oscillatory behaviour.

### 4.4. Implementation of the motor model into the ADC system

To combine the ADC system description and the dynamical model describing the motor, we use equation (15) to describe the position of the ADC rotor wheel. To determine $\theta_m$, we return to the motor torque description of equation (1),

$$\frac{d\omega_m}{dt} = \frac{1}{J_m} (\tau_m - \tau_l - B_m\omega_m), \qquad (18)$$

where we have used the subscript $m$ to denote that the respective parameter is a property of the motor. The load torque $\tau_l$ acting on the motor is only determined by the state of the axial coupling, the torsion energy wound up in the coupling by the difference in the upper and lower position.

Ignoring the electrodynamics of the motor, we can summarise the dynamics of the electro-mechanical system as fol-

lows:

$$
\begin{aligned}
\frac{d\omega_m}{dt} &= \frac{1}{J_m} (\tau_m - K(\theta_m + N\theta_2) - B_m\omega_m), \\
\frac{d\theta_m}{dt} &= \omega_m, \\
\frac{d\omega_2}{dt} &= \frac{1}{\alpha} (\theta_m - \beta\omega_2 - \gamma\theta_2), \\
\frac{d\theta_2}{dt} &= \omega_2.
\end{aligned}
\qquad (19)
$$

Non-linearity is introduced by the position dependence of the motor torque curve, equation (2),

$$
\begin{aligned}
\tau = k_m \left[ -i_1 \sin(N_r\theta) + i_2 \cos(N_r\theta) \right] \\
- 2L_{f4}N_r \sin(4N_r\theta)i_f^2 \quad \text{(2 revisited)}
\end{aligned}
$$

and the electrodynamics of the motor described in equation (1),

$$
\begin{aligned}
\frac{di_1}{dt} &= -\frac{R}{L_0}i_1 + \frac{k_m}{L_0}\omega \sin(N_r\theta) + \frac{v_1}{L_0}, \\
\frac{di_2}{dt} &= -\frac{R}{L_0}i_2 - \frac{k_m}{L_0}\omega \cos(N_r\theta) + \frac{v_2}{L_0}.
\end{aligned}
\qquad \text{(1 revisited)}
$$

The simulations of the complete ADC system were only carried out through high resolution time evolution of the differential equations above, due to the limiting assumptions that need to be made to solve a non-linear system analytically and the more complex implementation that this would require. A complete list of the numerical values assumed for the model parameters is given in Appendix B.

### 4.5. Issues and resolution in reproducing the measured system response

To obtain the measured response of the ADC prototype, an input signal was provided to perform a full step – consisting

9

of 32 microsteps – every second. A phase current amplitude of 1.2 A and no holding current (i.e. 0.0 A) were set on the Phytron MCC-2 controller that was used to drive the stepper motor. The stepping rate was set to 1000 Hz. As a result, the electrical current signals approach a sinusoidal with a frequency of 7.8125 Hz. After the first quarter of the period, the signal amplitude on both phases was set to zero.

Fig. 11 shows the modelled system response to this signal. Fig. 12 shows the response to a similar input, but at a lower stepping rate of 100 Hz. The simulated model successfully reached a final equilibrium position at 0.285°, in both cases. Notably, there is little change in the system response when the cold or warm motor is considered. For a stepping rate of 1000 Hz, the input signal ends well before the ADC rotor has reached the desired location, but the impulse of the motor, combined with the inertia of the wheels, pushes the system to the desired position. We observe a small initial overshoot of the rotor position, which is reduced by the correcting feedback from the detent torque of the motor. Any oscillations are quickly damped by the counter-electromotive force.

Clearly, this simulation did not reproduce the oscillations shown in the measured system response, Fig. 9, from which $K$ and $B$ were derived in Section 4.3. Furthermore, any of the mid-step reversals and slowdowns do not appear. It appears that the model is not yet complete.

### 4.5.1. Stribeck friction

Up to now, we have only considered the simplest friction; viscous friction. When the system is continuously moving, this may be sufficient. However, the MICADO ADC comes to rest often and static friction effects may play an important role. The Stribeck friction model [32, 33] offers a slightly more advanced description of friction that is easy to implement numerically. We used the following definition,

$$\tau_f = \text{sgn}(\omega)\left\{\tau_c + (\tau_{\text{brk}} - \tau_c)\exp\left[-\left(\frac{\omega}{\omega_{\text{brk}}}\right)^2\right]\right\} + B\omega. \quad (20)$$

This equation describes the friction as a function of the angular velocity $\omega$, the coulomb friction torque $\tau_c$, and the breakaway torque $\tau_{\text{brk}}$. The initial friction is large, a sort of stickiness of the moving body. At velocities above the breakaway speed $\omega_{\text{brk}}$, the viscous friction starts to dominate the total friction. The difference between the required torque to start moving and the coulomb friction torque is known as the static friction or stiction torque.

We applied this friction model to the motor in our numerical model, such that the viscous friction term ($B_m\omega_m$) in equation (18) was substituted by $\tau_f$. Now, we could finally reproduce the type of oscillations that were observed in the real prototype, under the assumptions that $\tau_{\text{brk}} = 90$ mNm, $\omega_{\text{brk}} = 10$ deg/s and $\tau_c = 0$. Two simulated responses are illustrated in Figs. 13 and 14. Acquiring these results did require us to increase the viscous friction on the motor from the assumed $3.5 \times 10^{-3}$ mNm s deg$^{-1}$ to 0.84 mNm s deg$^{-1}$.

At lower stepping frequencies, the addition of Stribeck friction has the curious effect that the mechanism may get stuck for some time, before continuing the repositioning of the ADC rotor, see Fig. 14. At higher frequencies, the inertia of the heavy ADC rotor prevents this from occurring. However, at low stepping rates the ADC inertia can not help as much and the motor must build up the required energy to overcome the high friction regime.

This staircase response has also been observed in the ADC prototype during an exploration of suitable motor parameters, see Figs. 15 and 16. Similar to the simulations, this behaviour occurred at lower stepping rates. This observation provides strong evidence for the presence of significant static friction.

## 5. Discussion

The presence of harmonic oscillations suggest that the Stribeck friction model applies to a component in between the system input (the electrical signal) and the oscillator. So far, we have assumed that the oscillator was the axial coupling. It is then surprising that the dominant factor in the friction would be the motor and not the friction wheels of the mechanism. We hypothesise that the observed oscillations are, therefore, not actually an angular vibration of the ADC rotor wheel, but rather a consequence of how the Zettlex angular encoder is attached to the rotor, see Fig. 17. In the ADC prototype, the encoder is encased in an aluminium wire frame, and could therefore oscillate if the rotor is exposed to angular acceleration. A finite element analysis of this component can easily determine the credibility of this hypothesis.

Not only would this hypothesis be consistent with the observed behaviour, it also provides an enticing explanation for the wear and tear that was observed after accelerated lifetime tests of the ADC mechanism prototype [20]. If it is indeed the encoder itself that oscillates, then the static friction can apply to the interface between the roller and rotor wheels. Furthermore, in the modelled response, the precise value chosen for $\tau_{\text{brk}}$ strongly influences the final position that the mechanism obtains. Small variations along the wheel surface due to material inhomogeneity and driving current variations would then explain the wide distribution of the step sizes observed with the prototype.

Having successfully identified the dominant factors in the ADC system response, there remains one significant feature in the measured response that we have not been able to explain. After the powered stepping of the ADC mechanism has ended, but just before the damped harmonic oscillations, there is a significant backwards movement. We have not been able to reproduce this feature in any of our simulated responses. It appears unlikely that this is a form of backlash or an artefact of the way the encoder is connected to the ADC rotor. The slope of the position curve is as steep as the movement at the start of the system step, hinting at a powered response. Unfortunately, the exact temporal behaviour of the Phytron MCC-2 motor controller is not understood at the level that our models would require to reproduce this. We have attempted to measure the input currents of the motor using an oscilloscope, but the high frequency
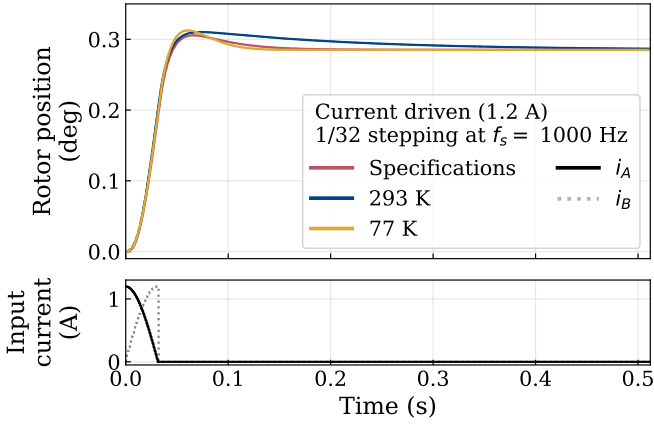
Figure 11: The simulated response of the combined motor and ADC mechanism model is shown in the top panel. Here, a single full step at 1/32 microstepping, with an current amplitude of 1.2 A and a stepping rate of 1000 Hz is simulated. The bottom panel shows this input signal.
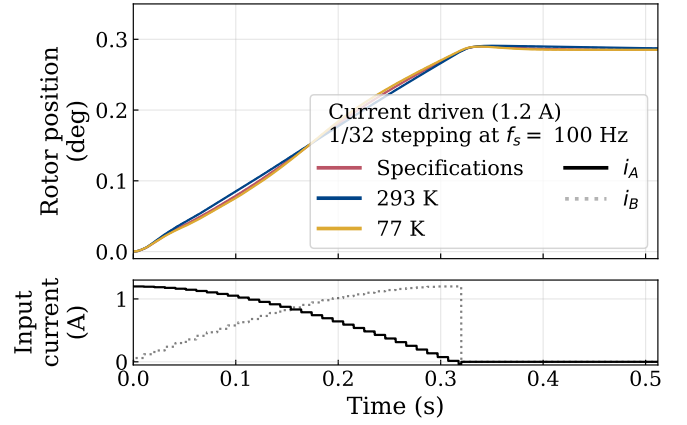


Figure 12: Similar to the left figure, but here at a much lower step frequency of 100 Hz, resulting in lower velocities and less overshoot.
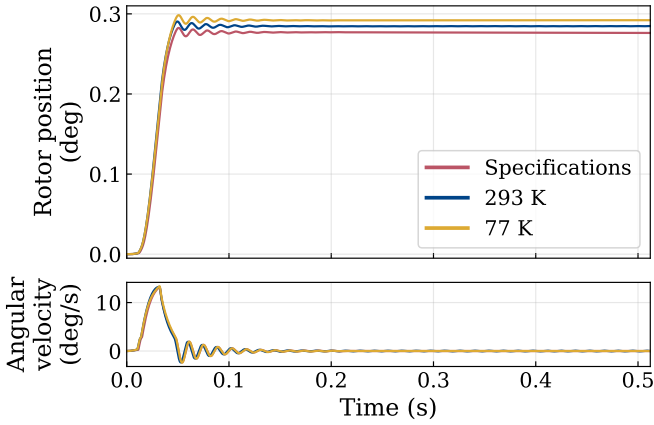


Figure 13: Including a Stribeck friction model, to include the effects of static friction, allows us to reproduce the oscillatory behaviour at the end of the ADC step in this simulated response. Here, the input signal is the same as in Fig. 11 and $\tau_{\text{brk}} = 90$ mNm, $\omega_{\text{brk}} = 10$ deg/s and $\tau_c = 0$.
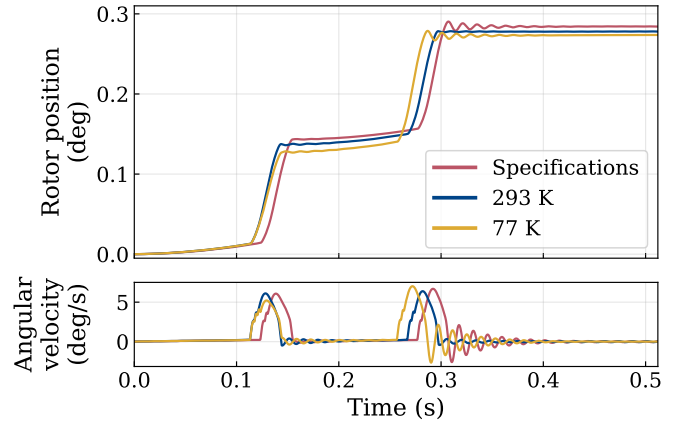


Figure 14: At low stepping frequencies (here: 100 Hz) the static friction included in the model produces a staircase like response. The input signal is the same as in Fig. 12 and $\tau_{\text{brk}} = 90$ mNm, $\omega_{\text{brk}} = 10$ deg/s and $\tau_c = 0$. The number of steps changes with the value of $\omega_{\text{brk}}$.
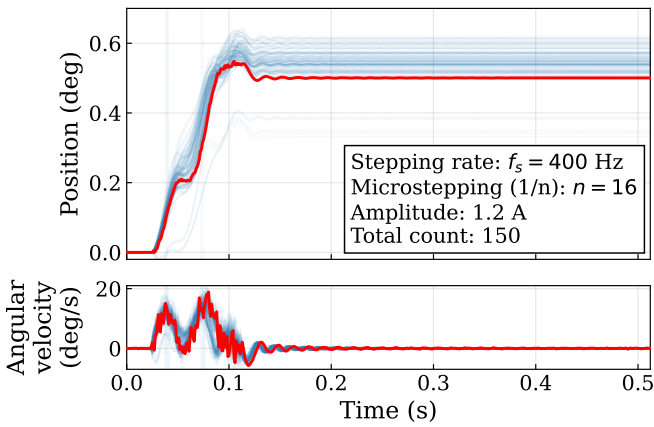


Figure 15: In this figure, the position and velocity of the ADC mechanism prototype is shown when a 400 Hz step frequency and 1/16 microstepping is used. The shape of the staircase response is somewhat different this time, but here too it looks like static friction.
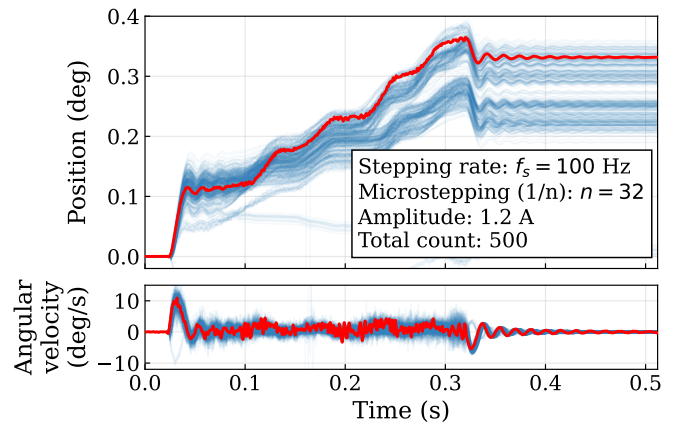


Figure 16: In this figure, the position and velocity of the ADC mechanism prototype is shown when a 100 Hz step frequency and 1/32 microstepping is used. The same staircase response occurs as in Fig. 14.
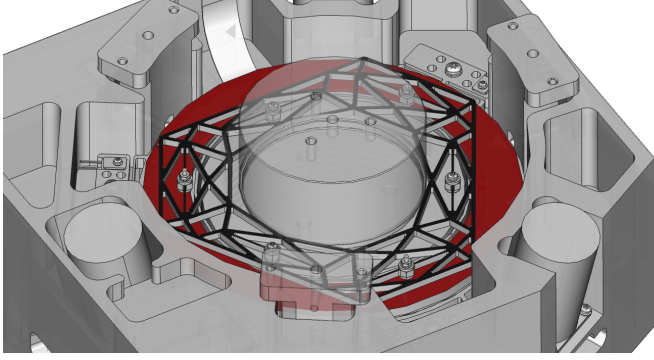
11

Figure 17: The Zettlex encoder rotor (red) is connected to the ADC rotor by an aluminium wire harness (black). During significant acceleration of the rotor wheel, it is possible that the inertial lag creates the observed harmonic oscillations. This would mean that these are not representative of the ADC rotor movement, but an artefact of the mechanical design.

pulse width modulation and other current shaping techniques made it difficult to understand the effective and relevant signal. Perhaps, the backwards rotation is a consequence of the current dropping back to zero after the full step has been completed, which would be limited by the electrical time constant of the motor wiring. More analysis is required to understand this backwards movement.

The comprehensive characterisation of the Phytron cryogenic stepper motor and subsequent successful modelling of the ADC mechanism is a starting point for the design of a suitable controller. This controller should take into account the different ADC tracking modes, predicted future reconfiguration and minimise wear and tear for an optimum lifetime. If the harmonic oscillations are indeed due to the wire harness through which the encoder was attached to the ADC prototype rotor, then these oscillations do not need to be considered for the controller design. The as-built MICADO ADC will have the encoder directly bolted to the ADC rotor, meaning that the observed oscillations should not occur at the observed frequency. Verification of this should be straight forward with the final assembled hardware.

The optical performance of the ADC would most benefit from a slow and controlled movement of the prisms, similar to the response presented in Fig. 12. Continuous correction of atmospheric dispersion would in that case only be a function of the step frequency. However, the non-negligible static friction of the roller and rotor wheels prohibits such a simple strategy and therefore a discretization of the ADC positioning is preferable. The residual dispersion due to the discrete positioning resolution is within the tolerances allowed by the instrument requirements [6]. Possibly, friction compensation techniques can be incorporated to improve performance [34–36]. Usually, effective compensation of friction requires closed-loop feedback with high resolution velocity sensors and minimal time delays. The Zettlex encoder included in the ADC design can record the position at 1 kHz rates, making it suitable for this purpose. In any case, the detailed design of a controller requires a new effort and is therefore left as future work in the development of the MICADO atmospheric dispersion corrector.

## 6. Conclusions

In this work, we have carried out an extensive characterisation and modelling effort to understand cryogenic performance of a Phytron VSS43.200.1.2 permanent magnet stepper motor in the context of the development of the MICADO atmospheric dispersion corrector. By matching the parameters of the differential equations of PMSM to measurable metrics, we were able to develop a representative physical model of the motor.

We find that there is no considerable difference in the delivered torque between the warm (293 K), cold (77 K) and as-specified stepper motor. A few per cent difference in the holding torque was observed, but small number statistics prevented us from concluding its significance. The primary difference in the cold and warm motor originated from the changed resistance of the PMSM wiring, leading to a longer electrical time constant.

With a representative PMSM model available, a dynamical model of the ADC mechanism was derived to model the temporal response. Values were assigned to the various parameters through a combination of by-design, empirical and estimated values. Comparisons with the measured prototype response were possible because of the high angular and temporal resolution of the encoder on the ADC rotor wheel. Only through the addition of static friction, in the form of a Stribeck friction model, were we able to reproduce and explain the measured response. Static friction prevents movement of the ADC rotor when the available torque is less than approximately 90 mNm.

The representative physical model of the motor and the actual behaviour of the ADC prototype have shown good agreement. As such, the motor model will also prove useful for any project in which commercial cryogenic stepper motors are considered, as literature on this topic has been sparse. Finally, in this work we have also highlighted some of the challenges in building an active cryogenic mechanism and illustrated a small part of the development of the MICADO ADC. The detailed design of the controller – a next step in the development process, has been made much easier with the results of this modelling effort.

### Data availability statement

Our code and most data are publicly available at https://gitlab.astro.rug.nl/born/Project-SMADC.

This repository contains the code to reproduce all figures in this report. Only a small subset of the video recordings, used for Section 3.3 and Appendix C, are included due to filesize constraints. The full set of data are available from the first author upon reasonable request.

## Appendix A. Derivation of the ADC system description without the PMSM

For this appendix, our objective is to find the angular output of the large rotor wheel as a function of the input angle of the motor axis $\theta_m$. To derive the equation of motion of the ADC mechanism, we will first consider the wheels only. The forces acting on these wheels are shown schematically in Fig. A.18. Wheel 1 is the motorised wheel and experiences an input torque $\tau_{\text{in}}$. Friction, inertia and the physical contact with the large wheel decrease the effective torque. We define the contact torque acting on wheel $i$ due to some arbitrary contact force as $\tau_{ci} = f_{ci} r_i$, where $f_{ci}$ is a force acting on the radius $r_i$ of wheel $i$. The contact force on one wheel should have an equal but opposite component acting on the wheel on the other side of the contact interface. The exact nature of this force is not important as we will only use it to be able to derive a single equation of motion for the complete system and it will drop out of the equations in the process.

Next, we define the rotation of the large wheel by $r_1\theta_1 = -r_2\theta_2$, and we assume that no stick-slip effects are occurring. With this, we can write down the four equations of motion for these four wheels:

$$
\begin{aligned}
\tau_{\text{in}} - J_1\ddot{\theta}_1 - B_1\dot{\theta}_1 + f_{c1}r_1 &= 0, \\
f_{c1}r_2 - J_2\ddot{\theta}_2 - B_2\dot{\theta}_2 + f_{c2}r_2 + f_{c3}r_2 &= 0, \\
f_{c2}r_3 - J_3\ddot{\theta}_3 - B_3\dot{\theta}_3 &= 0, \\
f_{c3}r_4 - J_4\ddot{\theta}_4 - B_4\dot{\theta}_4 &= 0,
\end{aligned}
\tag{A.1}
$$

where we have used the dot and double dot notation to denote the first and second order time derivative of $\theta$, respectively. As before, $J_i$ and $B_i$ denote the inertia and viscous friction coefficient of wheel $i$.

The three smaller wheels have an equal radius, so that we may write

$$
\theta_i = -\frac{r_2}{r_i}\theta_2 = -N\theta_2, \quad \text{with } i \in \{1, 3, 4\}, \tag{A.2}
$$

with $N$ as the gear ratio between the wheels.

To find the angular output of the large wheel, $\theta_2$, we use the previous two equations to find

$$
\tau_{\text{in}} + \left[N(J_1 + J_3 + J_4) + \frac{J_2}{N}\right]\ddot{\theta}_2 \\
+ \left[N(B_1 + B_3 + B_4) + \frac{B_2}{N}\right]\dot{\theta}_2 = 0 \tag{A.3}
$$

Equation (A.3) is the single equation of motion of the wheels.

The motor shaft is coupled to the first wheel by an axial coupling, which can act as a torsional spring. The coupling of the
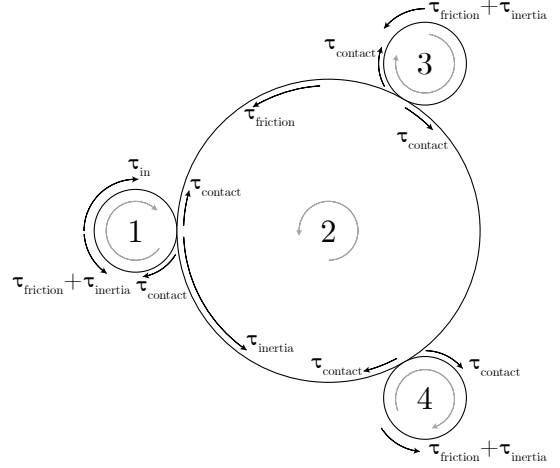


Figure A.18: The free body diagram of the prism pair mechanism. The motor and the motor coupling are not included in this diagram. The torque $\tau_{\text{in}}$ delivered by the motor comes into the system at roller 1. Wheel 2 is the rotor wheel and will contain the Amici prism. Wheels 3 and 4 are two supporting passive roller wheels. The size of the arrows has no relation to the real torque values.

motor shaft angular position, $\theta_m$, is related to the angular position of the first wheel, $\theta_1$, by

$$
\tau_m = K(\theta_{\text{in}} - \theta_1) = K(\theta_{\text{in}} + N\theta_2) \tag{A.4}
$$

Substitution of equation (A.4) into equation (A.3), gives the final equation of motion for the ADC mechanism.

$$
\left[N(J_1 + J_3 + J_4) + \frac{J_2}{N}\right]\ddot{\theta}_2 \\
+ \left[N(B_1 + B_3 + B_4) + \frac{B_2}{N}\right]\dot{\theta}_2 \\
+ KN\theta_2 = -K\theta_m \tag{A.5}
$$

Or more simply,

$$
\alpha\ddot{\theta}_2 + \beta\dot{\theta}_2 + \gamma\theta_2 = \theta_m, \tag{A.6}
$$

where we define

$$
\begin{aligned}
\alpha &= -\frac{N}{K}(J_1 + J_3 + J_4) - \frac{J_2}{KN}, \\
\beta &= -\frac{N}{K}(B_1 + B_3 + B_4) - \frac{B_2}{KN}, \\
\gamma &= -N.
\end{aligned}
$$

## Appendix B. Parameter values of the combined ADC and PMSM model

Table B.2 summarises the relevant parameters that were used in the modelling of the ADC system.

## Appendix C. Driving torque

An overview of the measured driving torque of the Phytron VSS43.200.1.2 motor is provided in Fig. C.19.
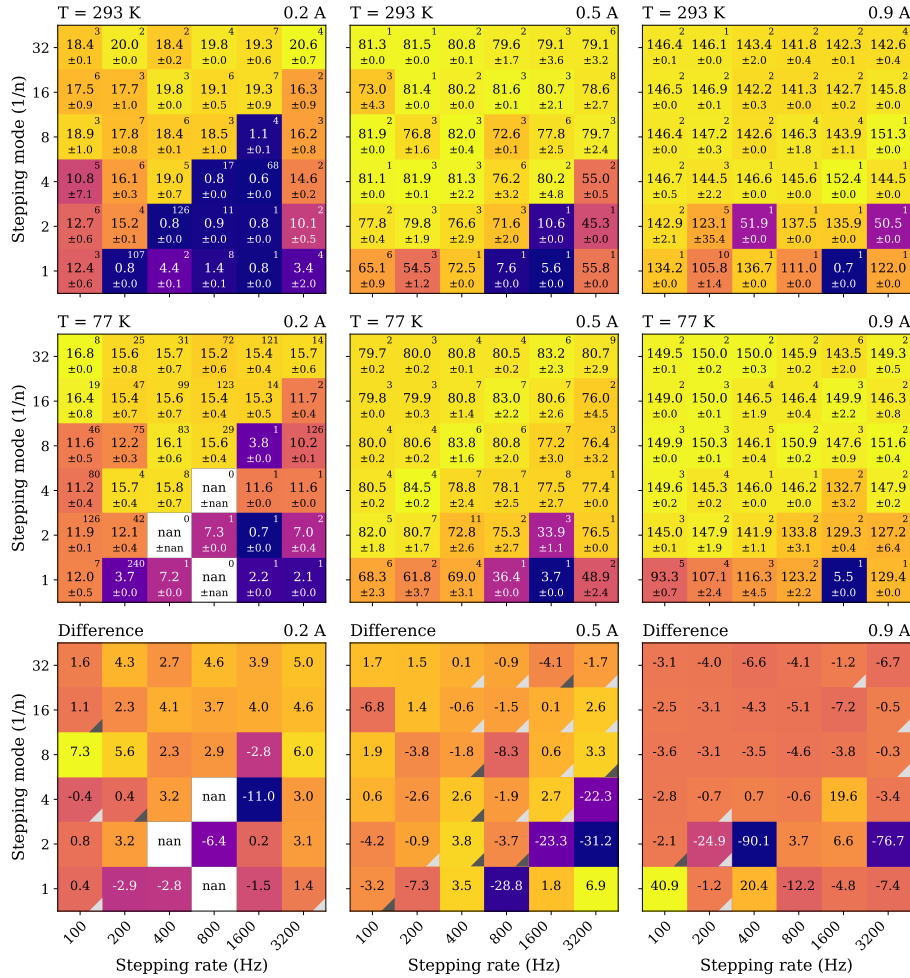
Figure C.19: Overview of the measured driving torques of the Phytron motor in millinewton meter. The rows correspond to measurements at room temperature (293 K), cryogenic conditions (77 K) and the difference between the two. The applied current changes with the column. In each subfigure, the stepping rates are varied along the x-axis and the stepping mode is varied along the y-axis. Within the cells of the first and second row, the mean of the measured peak driving torques is provided in the center, with the standard deviation below. The small value in the top right corner of each cell provides the number of maxima determined from the time-position curves. In the third row, some cells contain a light grey or dark grey triangle. These indicate whether the measured difference is within the standard deviation of one of the measurements or within the sum of the two standard deviations, providing a measure for the significance of the difference. Finally, a constant current frequency can be followed by inspecting the cells along a diagonal line – from lower left to upper right – in accordance with equation (12).

# References

[1] R. Davies, J. Schubert, M. Hartl, et al., MICADO: first light imager for the E-ELT, in: C. J. Evans, L. Simard, H. Takami (Eds.), Ground-based and Airborne Instrumentation for Astronomy VI, Vol. 9908 of Society of Photo-Optical Instrumentation Engineers (SPIE) Conference Series, 2016, p. 99081Z. arXiv:1607.01954, doi:10.1117/12.2233047.

[2] ESO, E-ELT Construction Proposal, https://www.eso.org/public/archives/books/pdf/book_0046.pdf, [Accessed: 2023-01-17] (Dec. 2011).

[3] R. Tamai, B. Koehler, M. Cirasuolo, F. Biancat-Marchet, M. Tuti, J.-C. González Herrera, S. Ramsay, Status of the ESO's ELT construction, in: H. K. Marshall, J. Spyromilio, T. Usuda (Eds.), Ground-based and Airborne Telescopes IX, Vol. 12182 of Society of Photo-Optical Instrumentation Engineers (SPIE) Conference Series, 2022, p. 121821A. doi:10.1117/12.2631613.

[4] J. A. van den Born, R. Romp, A. W. Janssen, R. Navarro, W. Jellema, E. Tolstoy, B. Jayawardhana, M. Hartl, The MICADO atmospheric dispersion corrector: optomechanical design, expected performance and calibration techniques, in: C. J. Evans, J. J. Bryant, K. Motohara (Eds.), Ground-based and Airborne Instrumentation for Astronomy IX, Vol. 12184 of Society of Photo-Optical Instrumentation Engineers (SPIE)

Conference Series, 2022, p. 121842W. arXiv:2207.02572, doi:10.1117/12.2628877.

[5] A. T. Young, Understanding astronomical refraction, The Observatory 126 (2006) 82–115.

[6] J. A. van den Born, W. Jellema, Quantification of the expected residual dispersion of the MICADO Near-IR imaging instrument, MNRAS 496 (4) (2020) 4266–4275. arXiv:2006.12132, doi:10.1093/mnras/staa1870.

[7] S. M. Pompea, F. Bartko, J. R. Houck, Cryogenic testing of stepper motors, in: Instrumentation in Astronomy IV, Vol. 331 of Society of Photo-Optical Instrumentation Engineers (SPIE) Conference Series, 1982, pp. 35–43. doi:10.1117/12.933437.

[8] R.-R. Rohloff, H. Baumeister, M. Ebert, N. Münch, V. Naranjo, Cryogenic actuators in ground-based astronomical instrumentation, in: J. Antebi, D. Lemke (Eds.), Astronomical Structures and Mechanisms Technology, Vol. 5495 of Society of Photo-Optical Instrumentation Engineers (SPIE) Conference Series, 2004, pp. 636–643. doi:10.1117/12.551114.

[9] S. Maurice, R. C. Wiens, M. Saccoccio, et al., The ChemCam Instrument Suite on the Mars Science Laboratory (MSL) Rover: Science Objectives and Mast Unit Description, SSRv 170 (1-4) (2012) 95–166, section 3.2.3. doi:10.1007/s11214-012-9912-2.

Table B.2: This table summarises the values as they were used in the presented results of Section 4. The motor parameters are summarised in Table 1.

| Param. | Value | Unit | Description |
|---|---|---|---|
| $m_1$ | 0.033 | kg | Mass of wheel 1 |
| $m_2$ | 4.6 | kg | Mass of wheel 2 |
| $m_3$ | 0.033 | kg | Mass of wheel 3 |
| $m_4$ | 0.033 | kg | Mass of wheel 4 |
| $r_1$ | 0.016 | m | Radius of wheel 1 |
| $r_2$ | 0.101 | m | Radius of wheel 2 |
| $r_3$ | 0.016 | m | Radius of wheel 3 |
| $r_4$ | 0.016 | m | Radius of wheel 4 |
| $J_1$ | $4.22 \times 10^{-6}$ | kg m$^2$ | Inertia of wheel 1: $J = mr^2/2$ |
| $J_2$ | $2.35 \times 10^{-2}$ | kg m$^2$ | Inertia of wheel 2: $J = mr^2/2$ |
| $J_3$ | $4.22 \times 10^{-6}$ | kg m$^2$ | Inertia of wheel 3: $J = mr^2/2$ |
| $J_4$ | $4.22 \times 10^{-6}$ | kg m$^2$ | Inertia of wheel 4: $J = mr^2/2$ |
| $B_1$ | 0 | Nms | Viscous friction on wheel 1 |
| $B_2$ | 0.661 | Nms | Viscous friction on wheel 2 |
| $B_3$ | 0 | Nms | Viscous friction on wheel 3 |
| $B_4$ | 0 | Nms | Viscous friction on wheel 4 |
| $N$ | 6.3125 | | Gear ratio |
| $K_2$ | 4836 | Nm rad$^{-1}$ | Torsion constant as seen on the rotor |
| $K_c$ | 121.36 | Nm rad$^{-1}$ | Torsion constant of the axial coupling; $K_c = K_2/N^2$ |
| $\alpha$ | $-3.13 \times 10^{-5}$ | ms$^{-2}$ | Defined in equation (15) |
| $\beta$ | $-8.63 \times 10^{-4}$ | ms$^{-1}$ | Defined in equation (15) |
| $\gamma$ | $-6.3125$ | | Defined in equation (15) |
| $J_m$ | $7.7 \times 10^{-6}$ | kg m$^2$ | Inertia of the motor rotor |
| $B_m$ | $4.8 \times 10^{-2}$ | Nms | Viscous friction of the motor rotor |
| $\tau_{\text{brk}}$ | 0.09 | Nm | Breakaway torque |
| $\omega_{\text{brk}}$ | 0.175 | rad/s | Breakaway velocity |
| $\tau_c$ | 0 | Nm | Coulomb friction |

[10] J. Schmidt, W. Greg, Development and testing of a high compact stepper motor mechanism, in: E. A. Boesiger (Ed.), Proceedings of the 41st Aerospace Mechanisms Symposium, no. NASA/CP-2012-217653, 2012, pp. 167–173.

[11] S. Hayoz, L. Blecha, S. Liberatoscioli, F. Rottmeier, T. Würgler, M. Charif, A. Martinez, Miniaturised stepper motors for space applications, in: 19th European Space Mechanisms and Tribology Symposium, 2021.

[12] Phytron, VSS / VSH Stepper Motor - For Applications up to Ultra-High-Vacuum - Data Sheet, dS-074-A016 EN (5 2022).

[13] Phytron, phySPACE™ – Stepper Motor Series for Space applications, Standard and Customised Solutions – Data Sheet, dS-086-A013 EN (9 2019).

[14] C. de Jonge, M. Eggens, A. C. T. Nieuwenhuizen, A. Detrain, H. Smit, P. Dieleman, Cryogenic actuator testing for the SAFARI ground calibration setup, in: R. Navarro, C. R. Cunningham, E. Prieto (Eds.), Modern Technologies in Space- and Ground-based Telescopes and Instrumentation II, Vol. 8450 of Society of Photo-Optical Instrumentation Engineers (SPIE) Conference Series, 2012, p. 84504D. doi:10.1117/12.927095.

[15] I. Arend, M. Schoele, U. Ruppert, Z. Szücs, Cryogenic motors for Herschel/PACS and James Webb/MIRI and NIRSPEC, in: 14th European Space Mechanisms and Tribology Symposium, ESA Special Publication, 2011, pp. 379–383. doi:10.1117/12.927095.

[16] M. Eggens, D. van Loon, H. P. Smit, W. Jellema, P. Dieleman, A. Detrain, M. Stokroos, A. C. T. Nieuwenhuizen, Optimization and Verification of a Brushless DC-Motor for Cryogenic Mechanisms, in: L. Ouwehand (Ed.), 15th European Space Mechanisms and Tribology Symposium, Vol. 718 of ESA Special Publication, 2013, p. 55.

[17] E. Ma, H. Wu, Y. Li, Development and testing of a cryogenic induction motor with a novel dewar structure, Cryogenics 116 (2021) 103283. doi:https://doi.org/10.1016/j.cryogenics.2021.103283. URL https://www.sciencedirect.com/science/article/pii/S0011227521000412

[18] P. Pathak, O. Guyon, N. Jovanovic, J. Lozi, F. Martinache, Y. Minowa, T. Kudo, H. Takami, Y. Hayano, N. Narita, A High-precision Technique to Correct for Residual Atmospheric Dispersion in High-contrast Imaging Systems, PASP 128 (970) (2016) 124404. arXiv:1608.07252, doi:10.1088/1538-3873/128/970/124404.

[19] J. A. van den Born, W. Jellema, E. Dijkstra, Demonstration of an imaging technique for the measurement of PSF elongation caused by Atmospheric Dispersion, MNRAS 512 (4) (2022) 5812–5822. arXiv:2112.01284, doi:10.1093/mnras/stac845.

[20] J. A. van den Born, The MICADO Atmospheric Dispersion Corrector, Ph.D. thesis, University of Groningen, submitted and under assessment (Apr. 2023).

[21] F. Khorrami, P. Krishnamurthy, H. Melkote, Modeling and Adaptive Nonlinear Control of Electric Motors, Engineering online library, Springer, 2003. URL https://books.google.nl/books?id=4XCM4iSS6LgC

[22] M. Bodson, J. Chiasson, R. Novotnak, R. Rekowski, High-performance nonlinear feedback control of a permanent magnet stepper motor, IEEE Transactions on Control Systems Technology 1 (1) (1993) 5–14. doi:10.1109/87.221347.

[23] V. Athani, Stepper Motors : Fundamentals, Applications And Design, New Age International (P) Ltd., Publishers, 1997. URL https://books.google.nl/books?id=0m8NTozFZL8C

[24] P. Acarnley, Stepping Motors: A Guide to Theory and Practice, IEE control engineering series, Institution of Electrical Engineers, 2002. URL https://books.google.nl/books?id=zOBmXKh-OicC

[25] J. Buck, W. Hayt, Engineering Electromagnetics, McGraw-Hill Education, 2011. URL https://books.google.nl/books?id=XeaHcgAACAAJ

[26] R. A. Matula, Electrical resistivity of copper, gold, palladium, and silver, JPCRD 8 (4) (1979) 1147–1298. doi:10.1063/1.555614.

[27] J. Charmant, Kinovea (version 0.8.15) (2006). URL https://www.kinovea.org

[28] P. Virtanen, R. Gommers, T. E. Oliphant, M. Haberland, T. Reddy, D. Cournapeau, E. Burovski, P. Peterson, W. Weckesser, J. Bright, S. J. van der Walt, M. Brett, J. Wilson, K. J. Millman, N. Mayorov, A. R. J. Nelson, E. Jones, R. Kern, E. Larson, C. J. Carey, İ. Polat, Y. Feng, E. W. Moore, J. VanderPlas, D. Laxalde, J. Perktold, R. Cimrman, I. Henriksen, E. A. Quintero, C. R. Harris, A. M. Archibald, A. H. Ribeiro, F. Pedregosa, P. van Mulbregt, SciPy 1.0 Contributors, SciPy 1.0: Fundamental Algorithms for Scientific Computing in Python, Nature Methods 17 (2020) 261–272. doi:10.1038/s41592-019-0686-2.

[29] J. R. Dormand, P. J. Prince, A family of embedded runge-kutta formulae, Journal of Computational and Applied Mathematics 6 (1980) 19–26.

[30] E. Hairer, G. Wanner, Solving ordinary differential equations ii. stiff and differential-algebraic problems, Springer Verlag Series in Comput. Math. 14 (01 1996). doi:10.1007/978-3-662-09947-6.

[31] R. Kieburtz, The step motor–the next advance in control systems, IEEE Transactions on Automatic Control 9 (1) (1964) 98–104. doi:10.1109/TAC.1964.1105628.

[32] R. Stribeck, Die wesentlichen eigenschaften der gleit-und rollenlager, Zeitschrift des Vereines Deutscher Ingenieure 46 (1902) 1341–1348.

[33] F. Marques, P. Flores, J. Pimenta Claro, H. M. Lankarani, A survey and comparison of several friction force models for dynamic analysis of multibody mechanical systems, Nonlinear Dynamics 86 (3) (2016) 1407–1443.

[34] B. Armstrong-Hélouvry, P. Dupont, C. C. De Wit, A survey of models, analysis tools and compensation methods for the control of machines with friction, Automatica 30 (7) (1994) 1083–1138.

[35] H. Olsson, K. Åström, C. Canudas de Wit, M. Gäfvert, P. Lischinsky, Friction models and friction compensation, European Journal of Control 4 (3) (1998) 176–195. doi:https://doi.org/10.1016/S0947-3580(98)70113-X. URL https://www.sciencedirect.com/science/article/pii/S094735809870113X

[36] W. Ruan, Q. Dong, X. Zhang, Z. Li, Friction compensation control of electromechanical actuator based on neural network adaptive sliding mode, Sensors 21 (4) (2021) 1508.